Graphene Terahertz Plasmons: A Combined Transmission Spectroscopy and Raman Microscopy Study

Article *in* ACS Photonics · June 2017

DOI: 10.1021/acsphotonics.7b00384

CITATIONS
16

READS
88

6 authors, including:

Khwanchai Tantiwanichapan
Boston University
18 PUBLICATIONS **226** CITATIONS
SEE PROFILE

Habibe Durmaz
Karamanoglu Mehmetbey Üniversitesi
25 PUBLICATIONS **264** CITATIONS
SEE PROFILE

Yuyu Li
Boston University
22 PUBLICATIONS **178** CITATIONS
SEE PROFILE

Anna K Swan
Boston University
186 PUBLICATIONS **6,750** CITATIONS
SEE PROFILE

ACS Photonics

Article

pubs.acs.org/journal/apchd5

Graphene Terahertz Plasmons: A Combined Transmission Spectroscopy and Raman Microscopy Study

Khwanchai Tantiwanichapan,[†,‡,⊥] Xuanye Wang,[†,⊥] Habibe Durmaz,[†,§] Yuyu Li,[†] Anna K. Swan,[†] and Roberto Paiella*[,†]

[†]Department of Electrical and Computer Engineering and Photonics Center, Boston University, 8 Saint Mary's Street, Boston, Massachusetts 02215, United States

[‡]National Electronics and Computer Technology Center, 112 Khlong Luang, Pathum Thani, Thailand 12120

[§]Department of Electrical and Electronics Engineering, Recep Tayyip Erdogan University, Rize, Turkey 53100

Supporting Information

ABSTRACT: Graphene provides a promising materials platform for fundamental studies and device applications in plasmonics. Here we investigate the excitation of THz plasmon polaritons in large-area graphene samples on standard oxidized silicon substrates, via diffractive coupling from an overlying periodic array of metallic nanoparticles. Pronounced plasmonic absorption features are measured, whose frequencies can be tuned across a large portion of the THz spectrum by varying the array period. At the same time, the ability to tune these resonances actively via electrostatic doping is found to be strongly limited by the presence of large carrier density variations across the sample area induced by the underlying SiO_2, which are measured directly by Raman microscopy. These results highlight the importance of minimizing charge "puddles" in graphene plasmonic devices, e.g., through the use of more inert substrates, in order to take full advantage of their expected dynamic tunability for applications in THz optoelectronics.

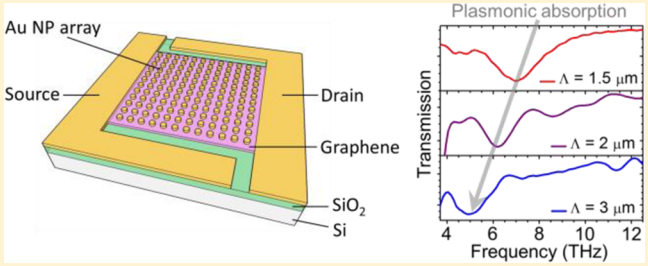

KEYWORDS: *graphene, terahertz photonics, plasmonics*

Graphene is a relatively new material for plasmonics research, with several distinctive and favorable properties.[1,2] Collective oscillations of the electron (or hole) gas in two-dimensional graphene sheets can produce guided electromagnetic waves with strong subwavelength confinement and reasonably large propagation lengths. For typical graphene carrier densities of several 10^{12} cm^{-2}, the resulting plasmonic resonances occur at mid-infrared and terahertz frequencies, as opposed to the visible or near-infrared excitations of traditional plasmonic nanostructures based on noble metals. Therefore, graphene plasmon polaritons (GPPs) provide a promising platform to extend the reach of plasmonic science and technology to longer and longer wavelengths. Furthermore, because the carrier density of graphene can be controlled through the application of a gate voltage, the plasmonic dispersion curves and resonance wavelengths are in principle dynamically tunable, which can add significant flexibility and functionality for device applications. As a result of these favorable properties, GPPs have become the subject of extensive theoretical and experimental studies in recent years.[1−19] Several device applications have also been proposed and investigated, including photodetectors,[20−22] optical modulators,[6,23] light emitters,[24−27] and biosensors.[28,29]

In the present work, we consider a particularly simple configuration for the study of THz GPPs, consisting of a continuous, large-area graphene sheet transferred onto an oxidized silicon substrate and then coated with a periodic array of metallic nanoparticles (NPs). Sharp plasmonic resonances are measured via transmission spectroscopy, associated with the diffractive scattering of the incident light by the NP array into GPPs. By varying the array period, the frequency of these grating-coupled plasmonic excitations is tuned across a wide portion of the THz spectrum, in good agreement with a standard model for the GPP dispersion. At the same time, however, the measured resonance frequencies are found to exhibit a much weaker dependence on gate voltage than expected based on the same model, even as the average carrier density in the graphene sheet is increased to relatively large values of several 10^{12} cm^{-2}. To explain these observations, Raman microscopy is employed to measure the local carrier density as a function of position, showing a large variance across the sample area for fixed gate voltage (attributed to the charged impurities that are commonly found in SiO_2/Si substrates). Since the oscillator strength for light absorption by GPPs also depends on carrier density, the plasmonic absorption spectrum measured across the entire sample at each gate voltage is dominated by the regions where such oscillator

Received: April 13, 2017
Published: June 26, 2017

DOI: 10.1021/acsphotonics.7b00384
ACS Photonics 2017, 4, 2011−2017

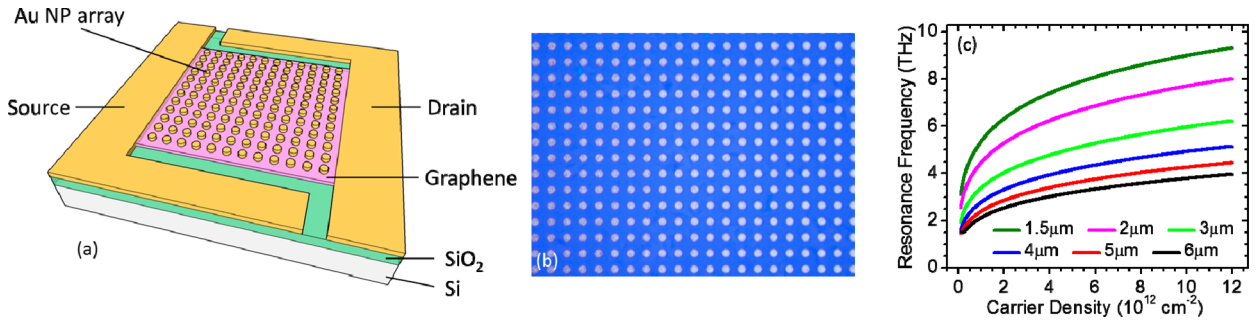

Figure 1. (a) Schematic illustration of the device geometry investigated in this work. (b) Top-view optical micrograph of a device with array period $\Lambda = 6\ \mu$m. (c) Calculated resonance frequency of grating-coupled GPPs, plotted as a function of carrier density N for different values of Λ.

strength is maximum. The key conclusion is that control of the carrier density uniformity is crucially important, especially in large-area samples, in order to take full advantage of the dynamic tunability of GPPs.

GRAPHENE PLASMON POLARITONS

The plasmonic dispersion properties of a continuous sheet of graphene can be computed by solving Maxwell's equations in the space immediately below and above the sheet (e.g., an oxidized Si substrate and air, respectively) and then applying the electromagnetic boundary conditions. In this formulation, graphene is described by means of its conductivity function $\sigma(\omega,\beta)$, where ω is the optical angular frequency and β is the wavenumber. If we consider the nonretarded regime ($\beta \gg \omega/c$) and use a simple Drude model for σ, the following dispersion relation is obtained:[3]

$$\beta(\omega) = \frac{\pi\hbar^2\varepsilon_0(\varepsilon_{r1}+\varepsilon_{r2})}{q^2E_f}\left(1+\frac{i}{\omega\tau}\right)\omega^2 \quad (1)$$

where ε_{r1} and ε_{r2} are the relative permittivities of the surrounding materials, τ is the relaxation time accounting for all relevant electronic scattering mechanisms, and E_f is the Fermi energy. The characteristic features of eq 1, including the ω^2 and $1/E_f$ dependence of the real part of β, are a general property of any two-dimensional electron gas (2DEG).[30] The dependence on carrier density per unit area N, however, is determined by the electronic band structure: in graphene, due to the conical dispersion near the Dirac points, $E_f = \hbar v_f\sqrt{\pi N}$ (where v_f is the Fermi velocity) so that $\beta \propto 1/\sqrt{N}$. In contrast, in traditional semiconductor 2DEGs with a parabolic energy dispersion, $\beta \propto 1/N$.

The propagation constant $\mathrm{Re}[\beta]$ of eq 1 can be substantially larger than the free-space wavenumber $k_0 = \omega/c$ at the same frequency, by 1 to 2 orders of magnitude depending on the relevant parameters. The implication is that the wavelength and transverse localization length of GPPs can be smaller than the free-space wavelength by the same factor, leading to extreme optical confinement. For the same reason, however, similar to surface plasmon polaritons in other 2DEGs or at planar metal−dielectric interfaces, GPPs in continuous films cannot be excited directly by incident radiation, whose in-plane wavevector is always smaller than k_0. Several different approaches have been explored to overcome this limitation. For the direct visualization of GPP propagation, near-field microscopy techniques have been employed to excite and monitor these surface waves,[8,9] by taking advantage of the highly evanescent optical fields that can be produced and collected by nanotips. To enable direct coupling to free-space radiation, as needed in typical device applications, subwavelength graphene features such as ribbons[6,13] or disks[7,11] have been used as a way to effectively eliminate the requirement of in-plane momentum conservation. Alternatively, the momentum mismatch between free-space radiation and GPPs in continuous films can be compensated by diffractive coupling with a periodic array. The latter approach has been demonstrated recently using graphene sheets transferred onto a surface relief grating[12,14,19] or patterned in the shape of a periodic lattice of discs[16] or holes (antidots).[15−17]

The device geometry used in the present work is illustrated in the schematic picture of Figure 1a and in the top-view optical micrograph of Figure 1b. Diffractive coupling in this geometry is provided by a square-periodic array of gold nanocylinders fabricated on a continuous sheet of graphene in the same lithography step as the source and drain metal contacts. This approach allows for a particularly simple fabrication process, as it does not require the transfer of graphene on a patterned substrate (where inhomogeneous strain fields may be produced leading to the formation of crystalline defects) or any complex shaping of the graphene sheet (where irregular and defective edges may be introduced). Thus, the device processing can be expected to have a minimal impact on the structural and electronic properties of the graphene sample supporting the GPPs.

In general, diffractive coupling relies on the ability of a grating of period Λ to shift the in-plane wavevector component of incident light by any integral multiple of $2\pi/\Lambda$. Assuming illumination at normal incidence, a GPP of angular frequency ω_{GPP} can therefore be excited if its propagation constant matches the shifted in-plane wavevector, i.e., $\mathrm{Re}[\beta(\omega_{GPP})] = 2\pi/\Lambda$ for first-order diffraction. Using eq 1, the following expression is then obtained for the grating-coupled GPP resonance frequency $f_{GPP} = \omega_{GPP}/(2\pi)$ (i.e., the frequency of the excited GPPs):

$$f_{GPP} = \frac{1}{2\pi}\sqrt{\frac{2q^2E_f}{\hbar^2\varepsilon_0(\varepsilon_{r1}+\varepsilon_{r2})\Lambda}} \quad (2)$$

According to this equation, f_{GPP} can be tuned geometrically by varying the array period Λ and dynamically by controlling the carrier density N and therefore the Fermi energy E_f through the gate voltage. To illustrate the resulting tuning range, in Figure 1c the GPP resonance frequency is plotted as a function of N for different values of Λ from 1.5 to 6 μm (the same values used in the experimental samples presented below). These traces were computed using eq 2 for a graphene sheet supported by a thin SiO_2 layer (of thickness $t_{OX} = 300$ nm) on a Si substrate. In

DOI: 10.1021/acsphotonics.7b00384
ACS Photonics 2017, 4, 2011−2017

this geometry, the effective permittivity of the underlying medium ε_{r1} is a weighted average of those of SiO_2 and Si (ε_{OX} and ε_{Si}, respectively), with the relative weights determined by the overlap factors of the GPP field intensity distribution with the two materials. For a GPP of propagation constant $\mathrm{Re}[\beta(\omega_{GPP})] = 2\pi/\Lambda \gg k_0$, the field intensity varies with distance z from the graphene plane approximately as $\exp(-4\pi|z|/\Lambda)$, which gives

$$\varepsilon_{r1} = \varepsilon_{Si}\exp(-4\pi t_{OX}/\Lambda) + \varepsilon_{OX}[1 - \exp(-4\pi t_{OX}/\Lambda)] \quad (3)$$

The materials parameters ε_{Si} and ε_{OX} are evaluated as a function of frequency using experimental data from the literature.[31] When combined with eq 2, this expression introduces an additional, weaker Λ dependence to f_{GPP}, which is included in the calculation results of Figure 1c. As illustrated by these traces, grating-coupled GPP resonances with tunable frequencies across the entire THz spectrum can be obtained using micrometer-scale array periods.

RESULTS AND DISCUSSION

The experimental samples are based on commercial graphene grown by chemical vapor deposition (CVD) on copper foil. Large-area films of this graphene material are transferred onto oxidized Si substrates using a supporting layer made of poly(methyl methacrylate) (PMMA), which is then thoroughly removed with an acetone bath followed by a dry anneal process. In order to enable gated transmission measurements at THz wavelengths without excessive free-carrier absorption, substrates based on lightly p-doped Si are employed, with a nominal resistivity of 1−10 Ω·cm. Prior to the transfer step, a small window is etched through the top SiO_2 layer, where the gate contact is deposited. Next, optical and Raman microscopy are used to identify rectangular sections of the transferred graphene film having minimal defect density and sufficiently large lateral dimensions (several 100 μm) for high-throughput optical transmission, which are then patterned by plasma ashing. Finally, the source−drain contacts and the NP array are fabricated simultaneously using electron-beam lithography, electron-beam deposition of a bilayer of 5 nm Cr and 60 nm Au, and liftoff. Several devices of different array period Λ were prepared, with an NP diameter approximately equal to $\Lambda/2$. Atomic force microscopy (AFM) images of these samples show continuous graphene coverage and relatively smooth surface morphology, with small nanometer-scale variations in surface height (see Supporting Information, Figure S1). Similar surface profiles are measured in graphene samples prepared with a variety of transfer techniques.[32]

The electrical characteristics of the resulting devices are illustrated in Figure 2, where the blue symbols show the room-temperature resistivity of a sample with a 2 μm NP-array period plotted as a function of gate voltage V_{gs}. The charge neutrality point of minimum conductance is found to occur at a relatively large positive voltage, $V_{gs} \equiv V_{CNP} \approx 30$ V, which indicates the presence of substantial p-type doping in the ungated graphene. This behavior is commonly observed in graphene samples on SiO_2[33] and is attributed to charge transfer from impurities in the substrate. The asymmetry in the resistivity data of Figure 2 (with the hole side featuring a larger slope compared to the electron side) can also be ascribed to the same phenomenon. To estimate the sample mobility, we employ a simple model for the graphene resistivity dependence on carrier density N (including both long- and short-range scattering),[34,35] where N is computed from the gate capacitor relation $qN = (\varepsilon_0\varepsilon_{OX}/t_{OX})(V_{gs} - V_{CNP})$ and listed in the top horizontal axis of Figure 2. The solid red line in the figure is a numerical fit based on this model applied to the hole side of the experimental data. A value of 1700 $cm^2/V/s$ is obtained for the hole mobility from this fit, which is quite high for CVD graphene deposited on SiO_2 using PMMA,[36] indicating very good overall sample quality. Similar values were estimated in all other devices developed in this work, including samples fabricated with the same procedure but without any NP array.

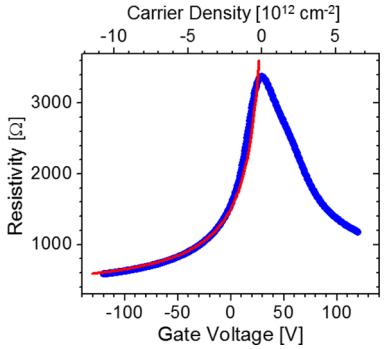

Figure 2. Electrical characterization results of a graphene sample coated with a 2-μm-period Au NP array. Blue symbols: Room-temperature resistivity measured as a function of gate voltage. The top horizontal axis shows the corresponding carrier density (negative values indicate holes). Solid red line: Numerical fit to the hole side of the experimental data based on the model discussed in refs 34 and 35, from which a hole mobility of 1700 $cm^2/V/s$ is inferred.

The far-infrared transmission spectra of the grating-coupled devices are measured using a Fourier transform infrared (FTIR) spectrometer equipped with a globar source, Mylar beamsplitter, and liquid-He-cooled Si bolometer. In these measurements, the samples are held at room temperature under vacuum, and their transmission spectra are recorded for different values of the applied gate voltage V_{gs}. At the same time, the resistivity between the source and drain contacts is constantly monitored to ensure the absence of any gate hysteresis and shift of the charge neutrality point, which are sometimes observed in similar devices on SiO_2 (particularly with the application of large gate voltages over extended periods of time).[37] Furthermore, to avoid dielectric breakdown in the SiO_2 layer, the leakage current I_{leak} between the source and gate contacts is also constantly monitored, and the gate voltage is not increased beyond the point where a superlinear increase in I_{leak} is observed. These considerations determine the maximum accessible value of V_{gs} for each measured sample. Finally, the transmission spectra are divided by the spectrum at the charge neutrality point to normalize out the spectral dependence of the FTIR system response and any features in the sample transmission that are not related to the graphene free-carrier distribution.

Representative results are shown in Figure 3a and b for two devices of array period Λ = 1.5 and 5 μm, respectively. Pronounced transmission dips are observed in both plots, whose amplitude increases monotonically with increasing gate voltage. As described in more detail below, the spectral positions of these features and their dependence on the array period are fully consistent with a picture of GPP excitation via diffractive coupling. For the 1.5-μm-period sample of Figure 3a, the measured transmission dips display a highly symmetric line shape centered around 7 THz, with a relatively large quality

DOI: 10.1021/acsphotonics.7b00384
ACS Photonics 2017, 4, 2011−2017

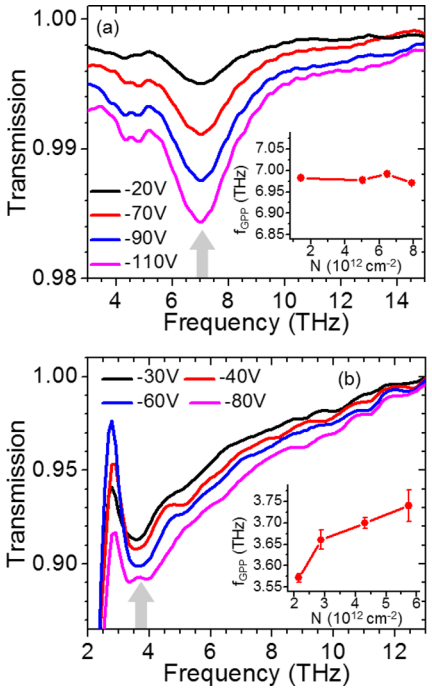

Figure 3. Normalized room-temperature transmission spectra of two devices with array period Λ = 1.5 μm (a) and 5 μm (b), for different values of the gate voltage $V_{gs} - V_{CNP}$ (listed in each panel). The arrows indicate the transmission dips due to grating-coupled GPP excitation. The inset in each panel shows the frequency of minimum transmission (obtained from a Gaussian fit of the experimental data) as a function of carrier density (estimated from $V_{gs} - V_{CNP}$ using the gate capacitor relation).

factor for THz GPP absorption of nearly 4. For the 5-μm-period device of Figure 3b, the plasmonic absorption peak is red-shifted to around 4 THz, near the low-frequency cutoff of the bolometer filter below 3 THz. In this frequency range, free-carrier absorption in the graphene sheet also produces a substantial contribution to the normalized transmission spectra, as evidenced by the slowly varying background of decreasing transmission with increasing wavelength superimposed to the plasmonic feature of Figure 3b. The insets of both panels of Figure 3 show the measured frequency of maximum GPP absorption f_{GPP} (obtained from a Gaussian fit of the experimental dips) as a function of carrier density N (estimated from $V_{gs} - V_{CNP}$ using the gate capacitor relation). For the 1.5-μm-period device, the resonance appears to be essentially constant with N over the entire range investigated. For the 5-μm-period device, a blue shift is observed as the carrier density is increased from 2 to 6 × 10^{12} cm^{-2}, in qualitative agreement with theoretical expectations. However, the magnitude of this frequency shift (about 0.2 THz) is significantly smaller than predictions based on the simulation results of Figure 1c (0.9 THz for the 5-μm-period device over the same carrier density range).

A similar behavior is observed in all samples developed in this work (see Supporting Information, Figure S2): in each device, increasing $|V_{gs}|$ has the effect of increasing the amplitude of the transmission dip, but does not change the absorption frequency by any appreciable amount, similar to the data shown in Figure 3. A summary of the measured resonance frequencies is presented in Figure 4, where panels (a)−(f) show the normalized transmission spectra of all devices near their maximum accessible gate voltage. The symbols in Figure 4g show the corresponding frequencies of minimum transmission, plotted as a function of array period Λ. As indicated by the solid line in the same figure, these data are in good agreement with the expected $\sim 1/\sqrt{\Lambda}$ dependence of f_{GPP}, which confirms the GPP origin of the measured transmission dips. In passing, it should be noted that micrometer-scale Au NPs also support localized surface-plasmon resonances at frequencies of about $c/(2nD)$,[38] where n is the substrate refractive index and D is the NP diameter. In our samples, where $D \approx \Lambda/2$, these resonances are in the mid-infrared range well above 10 THz and exhibit a $1/\Lambda$ dependence on array period. Therefore, we can rule out any impact of these resonances on the measured transmission spectra. The same considerations also apply to the lattice surface modes of the Au NP arrays.

More specifically, the solid line in Figure 4g was obtained by fitting the experimental data of f_{GPP} versus Λ with eqs 2 and 3, using the Fermi energy E_f as the only fitting parameter. The resulting value of E_f (0.24 eV) corresponds to a carrier density N = 4.1 × 10^{12} cm^{-2}. The implication is that, for all values of V_{gs} used in our GPP absorption measurements, there are regions in the graphene sheet where the local carrier density is close to this extrapolated value, and these regions tend to dominate the measured absorption spectra. To investigate this interpretation, we have used Raman microscopy to study the carrier density distribution in the experimental samples. In general, the Raman G-band and 2D-band peak centers are linearly shifted according to both strain and doping, but with different slopes, and thus can be used to analyze both effects.[39−41] Here we use the G band, measured at several

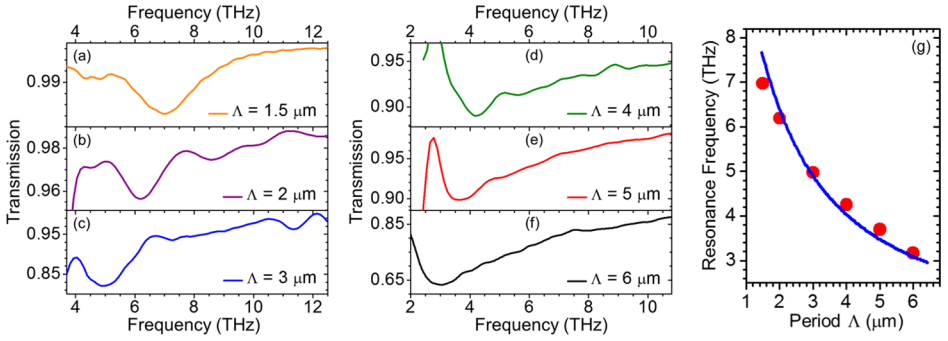

Figure 4. (a−f) Normalized room-temperature transmission spectra of six devices of different array period Λ, measured near their maximum accessible gate voltage. (g) Symbols: Frequencies of minimum transmission of the same devices (obtained from a Gaussian fit of the experimental data) plotted as a function of Λ. Solid line: Theoretical fit based on eqs 2 and 3.

DOI: 10.1021/acsphotonics.7b00384
ACS Photonics 2017, 4, 2011−2017

different locations as a function of gate voltage, with the samples again held at room temperature under vacuum. The results of this study for the 6-μm-period device are shown in Figure 5, where different colors correspond to different values of V_{gs} (listed above the top axis), and different data points plotted in each color were measured sequentially at different spots (each with an approximate size of 1 μm^2) across the sample area. Similar results were once again obtained with other samples, including graphene sheets without any NP array (see Supporting Information, Figure S3).

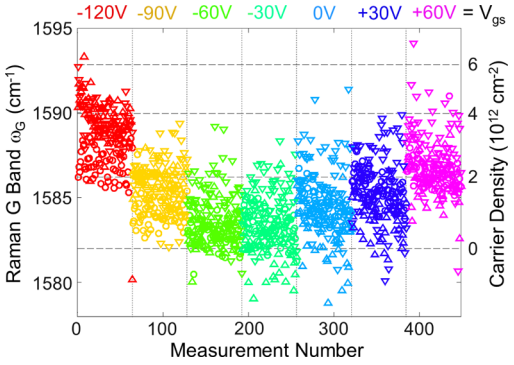

Figure 5. Raman G-band peak center (left axis) and corresponding estimated carrier density (right axis) measured at different spots in the 6-μm-period device for different values of the applied gate voltage V_{gs} (listed above the top axis). Different colors correspond to different values of V_{gs}. The measured spots are situated within three different unit cells of the NP array, indicated by different symbols in the plot.

The shape of the data set plotted in Figure 5 is clearly indicative of gate doping, with the average G-band peak center (and therefore the average carrier density) going through a minimum around $V_{gs} \approx -30$ V. Incidentally, this value is significantly different from the charge neutrality voltage obtained from the electrical measurements (near +30 V in this device). This difference, which we also observe in bare graphene samples, is attributed to photodoping induced by the Raman laser light involving charges from the SiO_2 substrate.[42,43] In any case, the key observation in the present context is the large variance in G-band peak center measured for each gate voltage, suggesting a proportionally large variance in local carrier density. For a more quantitative analysis, the strain-induced peak shifts have been removed following refs 39 and 41, so that the charge density at each data point could be estimated from the peak center. The results of this extrapolation are indicated on the right axis of Figure 5. It should be emphasized that some uncertainties exist in this analysis, particularly related to the subtraction of strain effects,[39,41] so that the resulting values of N are only approximate estimates. In fact, the relatively small rate at which the average carrier density in Figure 5 increases with increasing $|V_{gs} - V_{CNP}|$ suggests that these extrapolated values of N are likely lower bounds.

On the basis of these data, we conclude that carrier density variations δN on the order of $(2-3) \times 10^{12}$ cm^{-2} exist across the sample area for each applied value of the gate voltage. Charge "puddles" of similar magnitude have already been reported in unpatterned graphene samples on SiO_2[39,44,45] and can be attributed to the presence of charged impurities in the substrate, possibly compounded by small variations in the graphene–SiO_2 adhesion (see Figure S1). Under these conditions, the GPP dispersion properties can be expected to be substantially modified relative to the model of eq 1, which assumes a uniform charge distribution. In the simplest possible description, we can assume that local oscillations of the graphene electron (or hole) gas still follow eq 1, but with a position-dependent Fermi level E_f. In the presence of a diffraction grating, as in our samples, incident light will then be absorbed nonuniformly through the excitation of such charge oscillations at a frequency and with an efficiency that depend on the local carrier density. The resulting transmission spectra are therefore dominated by the sample regions where such grating-coupled GPP excitation is most efficient.

To elucidate the relationship between absorption strength and local carrier density in these samples, we begin by noting that the grating-coupled excitation of surface plasmon polaritons can be generally described using coupled-mode theory.[46] In this formulation, the absorption probability for incident light at resonance (i.e., at $\omega = \omega_{GPP}$) is given by

$$A = \frac{4\gamma_{rad}\gamma_{int}}{(\gamma_{rad} + \gamma_{int})^2} \approx \frac{4\gamma_{rad}}{\gamma_{int}} \quad (4)$$

where γ_{rad} and γ_{int} are, respectively, the rate at which plasmonic oscillations are excited through the absorption of the incident light and the rate at which the same oscillations are damped nonradiatively in the supporting medium. The approximate equality in eq 4 is derived in the limit of $\gamma_{rad} \ll \gamma_{int}$ (i.e., in the undercoupled regime), which can be expected to hold for typical, highly dissipative plasmonic systems. For any 2DEG including graphene, the damping rate $\gamma_{int} = v_g \mathrm{Im}[\beta]$ (where $v_g = \partial\omega/\partial \mathrm{Re}[\beta]$ is the plasmonic group velocity) can be computed using eq 1 as $\gamma_{int} = 1/(2\tau)$. The excitation rate γ_{rad} on the other hand mostly depends on the geometry and dielectric contrast of the diffraction grating, rather than the graphene materials properties. Therefore, we find that the absorption strength of eq 4 is simply proportional to (and thus varies with N as) the scattering lifetime τ. The resulting carrier-density dependence is quite complex, as it involves several different scattering mechanisms. For CVD-grown graphene on SiO_2, dc electrical measurements show that the relaxation lifetime τ rapidly decreases in the limits of both small and large N (due to the dominant contribution of impurity and surface-roughness scattering, respectively) and reaches a maximum value at an intermediate hole density of about $(3-4) \times 10^{12}$ cm^{-2}.[47]

These considerations suggest the following picture for the experimental findings presented above. As illustrated in Figure 5, for constant gate voltage V_{gs} the carrier density N (and therefore the scattering lifetime τ and the plasmonic absorption strength A) vary widely with position across the sample area. The incident light is then most strongly absorbed in the regions where N is in the "optimal" range of minimum damping near $(3-4) \times 10^{12}$ cm^{-2}. As a result, the spectral range of maximum plasmonic absorption is determined by such optimal values of the local carrier density. The numerical fit shown in Figure 4g and discussed previously is particularly significant in this respect. According to this fit, the frequencies of peak absorption f_{GPP} measured with six different samples of different array period Λ are all consistent with a carrier density N of about 4.1 $\times 10^{12}$ cm^{-2}, i.e., near the optimal range of maximum absorption strength. We emphasize that this interpretation is somewhat idealized, as it assumes that the plasmonic oscillations at each location in the graphene sheet depend only on the local carrier density, whereas in reality a more

DOI: 10.1021/acsphotonics.7b00384
ACS Photonics 2017, 4, 2011–2017

complex interplay between such oscillations across the sample area can be expected. It has also been argued that the GPP relaxation lifetime τ may be different from the scattering lifetime that limits the dc-transport mobility, as it originates from the nonlocal conductivity function at finite momentum and frequency.[48] Furthermore, the aforementioned uncertainties in the carrier density values extrapolated from the Raman maps do not allow for a quantitative evaluation of what fraction of the sample area contributes to the peak absorption as a function of V_{gs}. Nevertheless, the arguments just presented provide a consistent explanation for the limited gate tunability of the plasmonic absorption resonances observed in conjunction with large carrier density variations.

Finally, we compare this interpretation with the findings of prior experimental studies of GPPs in different device geometries. Broad gate tunability has been observed at mid-infrared wavelengths using nanoscale probes[8,9] or graphene structures with submicrometer lateral dimensions,[11,13] where carrier density inhomogeneities can be expected to have a limited impact. At THz frequencies, while tunable absorption features have also been reported,[6,7,15,17,18] they mostly involve carrier densities above the range accessible in the present devices, extending beyond 10^{13} cm^{-2} (in some cases introduced by chemical doping[7,15] or with an electrolyte top gate[6,18]). Furthermore, the measured blue shifts with increasing carrier density mostly involve a broadening of the absorption features toward higher frequencies. Therefore, these results can also be described in accordance with the picture presented above. As N is further and further increased, the fractional sample area of minimum GPP damping eventually decreases to the point where other regions featuring higher carrier densities begin to give a dominant contribution to the plasmonic absorption spectra. The characteristic charge "puddles" of graphene samples on SiO_2 are therefore most effective at limiting the tunability of THz GPPs in the low to intermediate doping regime (up to the mid 10^{12} cm^{-2} range), where the carrier density variance δN is comparable to the average value. Unfortunately, as illustrated in Figure 1c, this regime is also where the GPP resonance frequency is most sensitive to the local carrier density, and therefore where its tunability could potentially have the largest impact for device applications. The results of the present work then suggest that any progress toward these devices at THz frequencies will require addressing the large carrier density inhomogeneity of typical graphene samples. A promising avenue is the use of more inert substrates compared to SiO_2, such as hexagonal boron nitride, which can also provide significantly longer relaxation lifetimes and therefore spectrally narrower GPP resonances with lower propagation losses.[49,50]

■ ASSOCIATED CONTENT

Supporting Information

The Supporting Information is available free of charge on the ACS Publications website at DOI: 10.1021/acsphotonics.7b00384.

AFM surface profile of a grating-coupled graphene sample developed in this work; normalized transmission spectra of similar devices; Raman map of a graphene sample without any overlying nanoparticle array (PDF)

■ AUTHOR INFORMATION

Corresponding Author

*E-mail: rpaiella@bu.edu.

ORCID

Roberto Paiella: 0000-0002-7183-6249

Author Contributions

⊥K. Tantiwanichapan and X. Wang have contributed equally to this work.

Notes

The authors declare no competing financial interest.

■ ACKNOWLEDGMENTS

This work was supported by the National Science Foundation under Grant DMR-1308659. K.T. and H.D. acknowledge partial support by a Royal Thai Government Fellowship and by a Turkey Ministry of Education Fellowship, respectively.

■ REFERENCES

(1) Grigorenko, A. N.; Polini, M.; Novoselov, K. S. Graphene Plasmonics. *Nat. Photonics* **2012**, *6*, 749−758.

(2) Low, T.; Avouris, P. Graphene Plasmonics for Terahertz to Mid-Infrared Applications. *ACS Nano* **2014**, *8*, 1086−1101.

(3) Hwang, E. H.; Das Sarma, S. Dielectric Function, Screening, and Plasmons in Two-Dimensional Graphene. *Phys. Rev. B: Condens. Matter Mater. Phys.* **2007**, *75*, 205418.

(4) Jablan, M.; Buljan, H.; Soljačić, M. Plasmonics in Graphene at Infrared Frequencies. *Phys. Rev. B: Condens. Matter Mater. Phys.* **2009**, *80*, 245435.

(5) Koppens, F. H. L.; Chang, D. E.; García de Abajo, F. J. Graphene Plasmonics: A Platform for Strong Light−Matter Interactions. *Nano Lett.* **2011**, *11*, 3370−3377.

(6) Ju, L.; Geng, B.; Horng, J.; Girit, C.; Martin, M.; Hao, Z.; Bechtel, H. A.; Liang, X.; Zettl, A.; Shen, Y. R.; Wang, F. Graphene Plasmonics for Tunable Terahertz Metamaterials. *Nat. Nanotechnol.* **2011**, *6*, 630−634.

(7) Yan, H.; Li, X.; Chandra, B.; Tulevski, G.; Wu, Y.; Freitag, M.; Zhu, W.; Avouris, P.; Xia, F. Tunable Infrared Plasmonic Devices Using Graphene/Insulator Stacks. *Nat. Nanotechnol.* **2012**, *7*, 330−334.

(8) Chen, J.; Badioli, M.; Alonso-González, P.; Thongrattanasiri, S.; Huth, F.; Osmond, J.; Spasenović, M.; Centeno, A.; Pesquera, A.; Godignon, P.; Elorza, A. Z.; Camara, N.; García de Abajo, F. J.; Hillenbrand, R.; Koppens, F. H. L. Optical Nano-Imaging of Gate-Tunable Graphene Plasmons. *Nature* **2012**, *487*, 77−81.

(9) Fei, Z.; Rodin, A. S.; Andreev, G. O.; Bao, W.; McLeod, A. S.; Wagner, M.; Zhang, L. M.; Zhao, Z.; Thiemens, M.; Dominguez, G.; Fogler, M. M.; Castro Neto, A. H.; Lau, C. N.; Keilmann, F.; Basov, D. N. Gate-Tuning of Graphene Plasmons Revealed by Infrared Nano-Imaging. *Nature* **2012**, *487*, 82−85.

(10) Gao, W.; Shu, J.; Qiu, C.; Xu, Q. Excitation of Plasmonic Waves in Graphene by Guided-Mode Resonances. *ACS Nano* **2012**, *6*, 7806−7813.

(11) Fang, Z.; Thongrattanasiri, S.; Schlather, A.; Liu, Z.; Ma, L.; Wang, Y.; Ajayan, P. M.; Nordlander, P.; Halas, N. J.; García de Abajo, F. J. Gated Tunability and Hybridization of Localized Plasmons in Nanostructured Graphene. *ACS Nano* **2013**, *7*, 2388−2395.

(12) Zhu, X.; Yan, W.; Jepsen, P. U.; Hansen, O.; Mortensen, N. A.; Xiao, S. Experimental Observation of Plasmons in a Graphene Monolayer Resting on a Two-Dimensional Subwavelength Silicon Grating. *Appl. Phys. Lett.* **2013**, *102*, 131101.

(13) Yan, H.; Low, T.; Zhu, W.; Wu, Y.; Freitag, M.; Li, X.; Guinea, F.; Avouris, P.; Xia, F. Damping Pathways of Mid-Infrared Plasmons in Graphene Nanostructures. *Nat. Photonics* **2013**, *7*, 394−399.

(14) Gao, W.; Shi, G.; Jin, Z.; Shu, J.; Zhang, Q.; Vajtai, R.; Ajayan, P. M.; Kono, J.; Xu, Q. Excitation and Active Control of Propagating

DOI: 10.1021/acsphotonics.7b00384
ACS Photonics 2017, 4, 2011−2017

Surface Plasmon Polaritons in Graphene. *Nano Lett.* **2013**, *13*, 3698−3702.
(15) Yeung, K. Y. M.; Chee, J.; Yoon, H.; Song, Y.; Kong, J.; Ham, D. Far-Infrared Graphene Plasmonic Crystals for Plasmonic Band Engineering. *Nano Lett.* **2014**, *14*, 2479−2484.
(16) Zhu, X.; Wang, W.; Yan, W.; Larsen, M. B.; Bøggild, P.; Pedersen, T. G.; Xiao, S.; Zi, J.; Mortensen, N. A. Plasmon–Phonon Coupling in Large-Area Graphene Dot and Antidot Arrays Fabricated by Nanosphere Lithography. *Nano Lett.* **2014**, *14*, 2907−2913.
(17) Liu, P. Q.; Valmorra, F.; Maissen, C.; Faist, J. Electrically Tunable Graphene Anti-Dot Array Terahertz Plasmonic Crystals Exhibiting Multi-Band Resonances. *Optica* **2015**, *2*, 135−140.
(18) Jadidi, M. M.; Sushkov, A. B.; Myers-Ward, R. L.; Boyd, A. K.; Daniels, K. M.; Gaskill, D. K.; Fuhrer, M. S.; Drew, H. D.; Murphy, T. E. Tunable Terahertz Hybrid Metal-Graphene Plasmons. *Nano Lett.* **2015**, *15*, 7099−7104.
(19) Song, J.; Zhang, L.; Xue, Y.; Yang, Q.; Wu, S.; Xia, F.; Zhang, C.; Zhong, Y. L.; Zhang, Y.; Teng, J.; Premaratne, M.; Qiu, C. W.; Bao, Q. Efficient Excitation of Multiple Plasmonic Modes on Three-Dimensional Graphene: An Unexplored Dimension. *ACS Photonics* **2016**, *3*, 1986−1992.
(20) Vicarelli, L.; Vitiello, M. S.; Coquillat, D.; Lombardo, A.; Ferrari, A. C.; Knap, W.; Polini, M.; Pellegrini, V.; Tredicucci, A. Graphene Field-Effect Transistors as Room-Temperature Terahertz Detectors. *Nat. Mater.* **2012**, *11*, 865−871.
(21) Freitag, M.; Low, T.; Zhu, W.; Yan, H.; Xia, F.; Avouris, P. Photocurrent in Graphene Harnessed by Tunable Intrinsic Plasmons. *Nat. Commun.* **2013**, *4*, 1951.
(22) Cai, X.; Sushkov, A. B.; Jadidi, M. M.; Nyakiti, L. O.; Myers-Ward, R. L.; Gaskill, D. K.; Murphy, T. E.; Fuhrer, M. S.; Drew, H. D. Plasmon-Enhanced Terahertz Photodetection in Graphene. *Nano Lett.* **2015**, *15*, 4295−4302.
(23) Sensale-Rodriguez, B.; Yan, R.; Zhu, M.; Jena, D.; Liu, L.; Xing, H. G. Efficient Terahertz Electro-Absorption Modulation Employing Graphene Plasmonic Structures. *Appl. Phys. Lett.* **2012**, *101*, 261115.
(24) Rana, F. Graphene Terahertz Plasmon Oscillators. *IEEE Trans. Nanotechnol.* **2008**, *7*, 91−99.
(25) Otsuji, T.; Popov, V.; Ryzhii, V. Active Graphene Plasmonics for Terahertz Device Applications. *J. Phys. D: Appl. Phys.* **2014**, *47*, 94006.
(26) Liu, S.; Zhang, C.; Hu, M.; Chen, X.; Zhang, P.; Gong, S.; Zhao, T.; Zhong, R. Coherent and Tunable Terahertz Radiation from Graphene Surface Plasmon Polaritons Excited by an Electron Beam. *Appl. Phys. Lett.* **2014**, *104*, 201104.
(27) Brar, V. W.; Sherrott, M. C.; Jang, M. S.; Kim, S.; Kim, L.; Choi, M.; Sweatlock, L. A.; Atwater, H. A. Electronic Modulation of Infrared Radiation in Graphene Plasmonic Resonators. *Nat. Commun.* **2015**, *6*, 7032.
(28) Li, Y.; Yan, H.; Farmer, D. B.; Meng, X.; Zhu, W.; Osgood, R. M.; Heinz, T. F.; Avouris, P. Graphene Plasmon Enhanced Vibrational Sensing of Surface-Adsorbed Layers. *Nano Lett.* **2014**, *14*, 1573−1577.
(29) Rodrigo, D.; Limaj, O.; Janner, D.; Etezadi, D.; García de Abajo, F. J. G.; Pruneri, V.; Altug, H. Mid-Infrared Plasmonic Biosensing with Graphene. *Science* **2015**, *349*, 165−168.
(30) Stern, F. Polarizability of a Two-Dimensional Electron Gas. *Phys. Rev. Lett.* **1967**, *18*, 546.
(31) Palik, E. D. *Handbook of Optical Constants of Solids*; Academic Press, 1998; Vol. 1.
(32) Lee, H. C.; Liu, W.-W.; Chai, S.-P.; Mohamed, A. R.; Aziz, A.; Khe, C.-S.; Hidayah, N.; Hashim, M. S. U. Review of the Synthesis, Transfer, Characterization and Growth Mechanisms of Single and Multilayer Graphene. *RSC Adv.* **2017**, *7*, 15644−15693.
(33) Shi, Y.; Dong, X.; Chen, P.; Wang, J.; Li, L.-J. Effective Doping of Single-Layer Graphene from Underlying SiO_2 Substrates. *Phys. Rev. B: Condens. Matter Mater. Phys.* **2009**, *79*, 115402.
(34) Adam, S.; Hwang, E. H.; Galitski, V. M.; Das Sarma, S. A Self-Consistent Theory for Graphene Transport. *Proc. Natl. Acad. Sci. U. S. A.* **2007**, *104*, 18392−18397.
(35) Hong, X.; Zou, K.; Zhu, J. Quantum Scattering Time and Its Implications on Scattering Sources in Graphene. *Phys. Rev. B: Condens. Matter Mater. Phys.* **2009**, *80*, 241415.
(36) Kim, S. J.; Choi, T.; Lee, B.; Lee, S.; Choi, K.; Park, J. B.; Yoo, J. M.; Choi, Y. S.; Ryu, J.; Kim, P.; Hone, J.; Hong, B. H. Ultraclean Patterned Transfer of Single-Layer Graphene by Recyclable Pressure Sensitive Adhesive Films. *Nano Lett.* **2015**, *15*, 3236−3240.
(37) Wang, H.; Wu, Y.; Cong, C.; Shang, J.; Yu, T. Hysteresis of Electronic Transport in Graphene Transistors. *ACS Nano* **2010**, *4*, 7221−7228.
(38) Lu, X.; Han, J.; Zhang, W. Resonant Terahertz Reflection of Periodic Arrays of Subwavelength Metallic Rectangles. *Appl. Phys. Lett.* **2008**, *92*, 121103.
(39) Lee, J. E.; Ahn, G.; Shim, J.; Lee, Y. S.; Ryu, S. Optical Separation of Mechanical Strain from Charge Doping in Graphene. *Nat. Commun.* **2012**, *3*, 1024.
(40) Rémi, S.; Goldberg, B. B.; Swan, A. K. Charge Tuning of Nonresonant Magnetoexciton Phonon Interactions in Graphene. *Phys. Rev. Lett.* **2014**, *112*, 56803.
(41) Wang, X.; Tantiwanichapan, K.; Christopher, J. W.; Paiella, R.; Swan, A. K. Uniaxial Strain Redistribution in Corrugated Graphene: Clamping, Sliding, Friction, and 2D Band Splitting. *Nano Lett.* **2015**, *15*, 5969−5975.
(42) Kim, Y. D.; Bae, M.-H.; Seo, J.-T.; Kim, Y. S.; Kim, H.; Lee, J. H.; Ahn, J. R.; Lee, S. W.; Chun, S.-H.; Park, Y. D. Focused-Laser-Enabled p-n Junctions in Graphene Field-Effect Transistors. *ACS Nano* **2013**, *7*, 5850−5857.
(43) Tiberj, A.; Rubio-Roy, M.; Paillet, M.; Huntzinger, J.-R.; Landois, P.; Mikolasek, M.; Contreras, S.; Sauvajol, J.-L.; Dujardin, E.; Zahab, A. Reversible Optical Doping of Graphene. *Sci. Rep.* **2013**, *3*, 1−23.
(44) Rossi, E.; Das Sarma, S. Ground State of Graphene in the Presence of Random Charged Impurities. *Phys. Rev. Lett.* **2008**, *101*, 166803.
(45) Zhang, Y.; Brar, V. W.; Girit, C.; Zettl, A.; Crommie, M. F. Origin of Spatial Charge Inhomogeneity in Graphene. *Nat. Phys.* **2009**, *5*, 722−726.
(46) Yoon, J.; Seol, K. H.; Song, S. H.; Magnusson, R. Critical Coupling in Dissipative Surface-Plasmon Resonators with Multiple Ports. *Opt. Express* **2010**, *18*, 25702−25711.
(47) Nayfeh, O. M.; Birdwell, A. G.; Tan, C.; Dubey, M.; Gullapalli, H.; Liu, Z.; Reddy, A. L. M.; Ajayan, P. M. Increased Mobility for Layer-by-Layer Transferred Chemical Vapor Deposited Graphene/Boron-Nitride Thin Films. *Appl. Phys. Lett.* **2013**, *102*, 103115.
(48) Principi, A.; Vignale, G.; Carrega, M.; Polini, M. Impact of Disorder on Dirac Plasmon Losses. *Phys. Rev. B: Condens. Matter Mater. Phys.* **2013**, *88*, 121405.
(49) Zhang, K.; Yap, F. L.; Li, K.; Ng, C. T.; Li, L. J.; Loh, K. P. Large Scale Graphene/ Hexagonal Boron Nitride Heterostructure for Tunable Plasmonics. *Adv. Funct. Mater.* **2014**, *24*, 731−738.
(50) Woessner, A.; Lundeberg, M. B.; Gao, Y.; Principi, A.; Alonso-González, P.; Carrega, M.; Watanabe, K.; Taniguchi, T.; Vignale, G.; Polini, M.; Hone, J.; Hillenbrand, R.; Koppens, F. H. L. Highly Confined Low-Loss Plasmons in Graphene−Boron Nitride Heterostructures. *Nat. Mater.* **2014**, *14*, 421−425.

DOI: 10.1021/acsphotonics.7b00384
ACS Photonics 2017, 4, 2011−2017